Journal of Mathematics in Industry
a SpringerOpen Journal

RESEARCH Open Access

A mathematical characterization of anatomically consistent blood capillary networks

Marina Bertolini[1], Paola Causin[1*] and Cristina Turrini[1]

*Correspondence:
paola.causin@unimi.it
[1]Department of Mathematics, University of Milan, Milan, Italy

Abstract

Blood microcirculation is the site of control of tissue perfusion, blood-tissue exchange, and tissue blood volume. Despite the many irregularities, almost ubiquitously, one can recognize in microcirculation vessels a hierarchy of arterioles and venules, organized in tree-like structures, and capillary plexi, organized in net-like structures. Whilst for arterioles and venules it may be envisageable to obtain geometries needed for numerical simulations from imaging techniques, the size and numerosity of capillaries makes this task much more cumbersome. For this reason, it is interesting to study approaches to generate *in silico*-derived artifacts of capillary networks, even in view of machine-learning based approaches which require a large amount of samples for training. Artificial networks must correctly reflect proper metrics and topology, which in turn, will ensure with proper boundary conditions a physiological blood flux in the net and a sufficient nutrient distribution in the surrounding tissues. In this paper, we introduce the sequence of curves whose limit is the space filling Hilbert curve and we discuss its inherent properties and we obtain the backbone of the artificial capillary network from a suitable element of this sequence. The backbone represents a significant synthesis of basic metric features of the network and, in this context, its properties can be studied analytically. In this framework, the Hilbert curve is a malleable entity which allows to shape the backbone according to the physical indicators. In particular, two significant factors are shown to control the network topology and scaling: the iteration step of the Hilbert curve generation and the characteristic length of the REV, respectively. Based on the points we generate for a certain iteration step, we then obtain via spline interpolation a smoothed version of the curve, which fine–tunes the tortuosity. A volumetric construction is obtained building a tubular neighborhood of the backbone, whose metrics can be computed and tuned as well. Numerical simulations of the blood flow in the obtained geometry show the physical fields occurring in the artificial network.

Keywords: 3D space filling curves; Blood microcirculation; Capillary morphometry; Mathematical modelling; Numerical simulation

1 Content

The microcirculation is the collective name for the smallest (<150 μm in diameter) blood vessels. Microcirculatory vessels are the site of control of tissue perfusion, blood-tissue

exchange and tissue blood volume. Each of these functions can be associated, though not exclusively, with a specific type of microvascular segment: arterioles, capillaries and venules [1]. Microvessels do not generally form precise arrays in the tissue; rather, their spacing is non-uniform and their pathways are often tortuous [2]. Despite the irregularities in network structure, almost ubiquitously, arterioles and venules are organized in tree-like structures and capillary plexi in net-like structures. When performing numerical simulations, the geometry of larger vessels in microcirculation, corresponding to arterioles and venules, may be reconstructed from imaging. For example, in [3] the authors extracted from confocal laser microscopy of sliced sections of human brain hundreds of microvessels within a large cortex area of the human brain. The vessels corresponding to arteriole/venule level were clearly organized in tree-like structures. However, this operation is much more cumbersome when dealing with capillaries, as capillary beds are composed of thousands ($>10^4$) of tiny vessels with diameter ranging from 4 to 8 microns. For this reason, different studies have tackled this problem by *modeling* the capillary structures (see [4] for a review of the different approaches). Vessel-by-vessel descriptions tuned to a specific geometry are technically feasible but they are forcibly restricted to small tissue regions [5, 6]. Aside from this approach, the generation of synthetic capillary networks with equivalent properties allows to highlight common organizational features both *intra* and *interspecies* (see [7] for a discussion on topic). Simplified geometrical models describe capillaries as an idealized hierarchy of parallel vessels, as done in [8] for the eye retina capillaries. Whilst this representation can reasonably reproduce flow and pressure levels, it does not fully describe the real net-like organization of capillaries in its complexity. To model the net-like structure of capillary beds, some studies have used mathematical algorithms to generate coherent capillary meshes. In [9], a concentric circle mesh-like model was proposed to simulate capillaries in the rat retina. In [10], statistical algorithms were used to explore how the structural properties of the capillary bed influence the transport of blood through the human cerebral microvasculature. Sprouting angiogenesis algorithms have been used to generate capillary networks embedded in tumoral tissues (see, *e.g*, [11, 12]). In the recent work [13], a three-dimensional microvascular network representing a portion of the vasculature of the brain cortex is proposed, according to the mechanisms of angiogenesis, remodeling and pruning. In this model, stimuli are represented by oxygen levels and conducted responses in vessel walls. In [14], a representative cubic cell was introduced to compute equivalent quantities to be used in a further upscaling procedure: "*spaghetti-shaped*" capillaries with random orientations were embedded in the cell and a direct numerical simulation was performed. A similar approach was also pursued in [15], where a set of nodes were randomly seeded on a voxel to form a capillary network, on which upscaling was further performed. In [16–18], 3D capillary networks have been constructed using a Voronoi tessellation. A similar approach is considered also in [19] (see also the subsequent papers of the same authors and [7]), where the underlying structure of a 3D portion of the cerebral capillary net is obtained from a Voronoi dual mesh built from a tetrahedral Delaunay triangulation filling the space within a set of terminal arterioles and venules.

In this work we propose a technique to generate a net–like capillary geometry based on the observation of the space-filling nature of capillary networks at scales above a cut-off length of 25–75 μm [7]. Differently from [7, 17] and references therein, we base our construction of the network on the backbone obtained from successive approximations of

the 3D Hilbert curve [20], a mathematical construction which has the interesting property of displaying a range which, at the limit, fills an entire cube. In this framework, the Hilbert curve is a malleable entity which allows to shape the backbone to meet physical indicator parameters, according to the idea that the effective functioning of the vascular system depends sensitively on its geometrical characteristics. The cube forms a representative elementary volume (REV) and its characteristic length along with the iteration number in the generation of the backbone are chosen in order to meet appropriate scaling and length density/numerosity parameters. The main advantages of the present approach are: (a) an increased number of degrees of freedom which are being captured as opposed to other methods; (b) the fact that it can basically represent complex geometries by means of a recursive algorithm in a way that also complicated geometries could ultimately be mapped in a sequence of geometries obtained by suitable simple manipulations of piecewise constant curves; (c) the availability of different (possibly also distorted) configurations at a very low cost. This may turn to be useful in machine-learning based approaches, where one typically needs for training hundredths of samples that can be difficult to realistically obtain in the medical field. Artificial samples can be used in a first training phase, with a refinement based only on a limited number of real samples.

The paper is organized as follows: in Sect. 2 we present the construction of the backbone of the network via the approximants of the Hilbert curve and we compute its relative metrics which are relevant for our application; in Sect. 3 we present the construction of the volumetric neighborhood around the backbone with specific attention to the mean extravascular distance; in Sect. 4, we discuss the smoothing of the curve and the addition of segments to create loops, in order to obtain a realistic network; in Sect. 5 we present the results of 3D numerical simulations of the Stokes flow of blood in some instances of the network; eventually, in Sect. 6 we draw the conclusions.

2 Geometrical construction of artificial capillary networks: the backbone

In silico-built artifacts of capillary networks must reflect proper metrics and topology, which in turn, ensure a physiological blood flux in the net and a sufficient nutrient distribution in the surrounding tissues. Here below, we introduce the space filling curve called Hilbert curve and we discuss its inherent properties. In the present construction, the backbone of the artificial capillary network is obtained from a suitable element of the sequence of piecewise approximations of the Hilbert curve and constitutes the union of the centerlines of the volumetric construction of vessel branches. The backbone is, in general, a significant synthesis of basic metric features of the network and, in this context, its properties can be studied analytically. Two significant factors will be shown to control the network topology and scaling: the iteration step of the Hilbert curve generation and the characteristic length of the REV, respectively. In the following, we start recalling the construction of the sequence of piecewise linear curves whose limit is the Hilbert curve via an iterated procedure, then we deduce its geometrical properties at each step of the iteration.

2.1 Definition of the 3D Hilbert curve

According to [20], Sect. 2.8, letting $I = [0, 1]$, the Hilbert curve $H : I \to C$ is constructed as limit, for $n \to +\infty$, of a sequence $\Gamma := \{\Gamma_n\}$ of piecewise linear curves $\Gamma_n : I \to C$, embedded in a three dimensional cube C with edge l. Such a curve satisfies the topological

property of being *space filling* since it turns out to be *dense* in the cube C, and, being C compact, this implies that H is surjective, *i.e.*, $H(I) = C$. The density property implies that for each point P of the cube C and each open neighborhood U_P of P, it is possible to find a suitable step n of the iteration such that $\Gamma_n(I)$ intersects U_P. Moreover, as the sequence Γ is shown to be uniformly convergent and each Γ_n is continuous, also the Hilbert curve, which is its limit, is continuous. In this context, we consider finite n values and we use the corresponding curves Γ_n. Setting $n = 1$ we obtain Γ_1, which represents the basic pattern and we shall call from now on the *leit-motiv*; it can be obtained as follows (see [20] for an alternative arithmetic-analytic definition): one divides the cube C into 8 congruent sub-cubes -cutting it along the symmetry planes parallel to the faces- and takes the 8 centroids of these sub-cubes, which shall serve as the vertices of the curve. The leit-motiv is constructed by connecting the vertices with segments each of length $l_1 = \frac{l}{2}$, upon having established a traversal order of the points themselves (see Fig. 1). Setting now $n = 2$, to obtain Γ_2, one has to divide again each of the 8 sub-cubes as before so to obtain 8^2 sub-sub-cubes. Each set of the 8 centroids coming from the same sub-cube is connected by a curve L_i, $i = 1, \ldots, 8$, and represents a scaled transformation of the leit–motiv (see below for a detailed discussion of this point); each L_i is then connected to L_{i+1}, $i = 1, \ldots, 7$ by segments s_i (segment s_1 is shown in Fig. 2 for reference). Again, we see that $\Gamma_2(I)$ connects 8^2 nodes via 8×7 segments, whose length is $l_2 = \frac{l}{2^2}$, and 7 connecting arcs whose length is still l_2, hence 63 segments whose length is l_2. The method to get Γ_{n+1} from Γ_n is analog to the one to obtain Γ_2 from Γ_1. At step n the original cube is partitioned into 8^n sub-cubes.

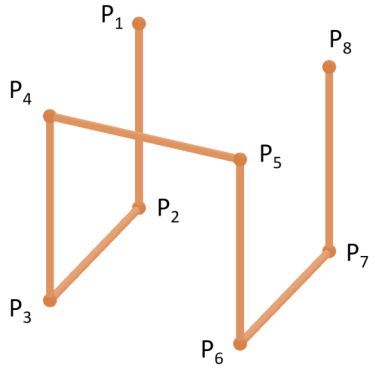

Figure 1 Leit-motiv of the Hilbert curve, coincident with the curve Γ_1 obtained at the first iteration. The order of traversal is indicated by the numbering of the vertices

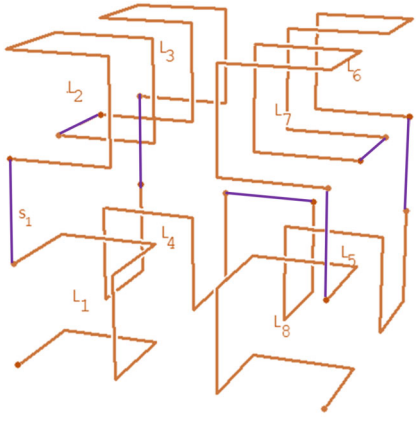

Figure 2 Curve Γ_2 obtained at the second iteration. The continuous polygonal curve is constructed from the leit-motivs L_i, $i = 1, \ldots, 8$, by connecting the last node of L_i with the first node of L_{i+1}, $i = 1, \ldots, 7$, with segment s_i (denoted by the violet color, for clarity only segment s_1 is annotated in the figure), modulo prior scaling/transformation of each leit-motiv

```
def hilbert3(n):
if n <= 0 then
    set [x, y, z]=0;
else
    [x_o, y_o]=hilbert3(n − 1);
    [x, y, z]=generatemotiv(x_o, y_o, z_o);
end
```

Algorithm 1: Recursive algorithm to generate the sequence $\{\Gamma_n\}$ of 3D space filling Hilbert curves

To obtain Γ_{n+1}, each of these sub-cubes is still partitioned in 8 sub-cubes into which is fitted a pattern which is a scaled transformation of Γ_n; the 8 patterns similar to Γ_n are then connected by 7 segments. At step n, $\Gamma_n(I)$ connects 8^n nodes via 8 patterns Γ_{n-1} and 7 connecting arcs whose length is $l_n = \frac{l}{2^n}$. Hence, with a computation by recursion, we get that $\Gamma_n(I)$ consists of $8^n - 1$ segments whose length is l_n.

The above iterative procedure is numerically implemented via the recursive Algorithm 1. Upon giving as an input the final desired iteration step n, the function iterates recursively; at each recursive call, the function `generatemotiv()` takes in input a pivoting point $[x_o, y_o, z_o]$, which is a vertex of the previous level leit-motivs and arranges around it a scaled/transformed (rotated, mirrored, translated) leit-motiv, generating the new vertex coordinates $[x, y, z]$. The vertices are eventually connected to form a continuous polygonal curve, the traversal order being implicit in the procedure itself. The base leit–motiv is built for $n = 1$.

According to the transformations implemented in the `generatemotiv()` function, in 3D one can generate more than 10^6 different sequences converging to different Hilbert curves which are anyways essentially equivalent from the metrical point of view, as shown in [21]. In this work we will limit ourselves to consider one specific instance of transformations, which is sufficient for our goals. To exemplify the procedure encoded `generatemotiv()`, we refer to the simplified 2D setting, its extension to the 3D case being similar. In this setting, the cube reduces to square which is divided in four quadrants (see Fig. 3, which shows the Hilbert curves obtained for n schematized with the dashed blue line and $n+1$, respectively). The basic leit-motiv is formed by the polygonal curve joining 4 vertices disposed symmetrically about the coordinate origin (dashed blue line). At each iteration, the leit-motivs in the quadrants are obtained from the original leit-motiv by the following transformations around the pivotal points (vertices) of the leit-motiv of the previous iteration (blue dots in Fig. 3): (1) reflection about the x axis and then rotation $\pi/2$ counterclockwise, translation and scaling (red curve, south-west quadrant); (2) translation and scaling (black curve, north-west quadrant); (3) translation and scaling (green curve, north-east quadrant); (4) rotation $\pi/2$ counterclockwise, translation and scaling (magenta curve, south-east quadrant). The traversal order of each transformed leit-motiv allows to form a continuous polygonal curve upon joining the end of and the beginning of the leit-motivs (dashed gray lines). We refer to [22] and [23] for efficient MATLAB implementations of the above construction in 2D and 3D, respectively.

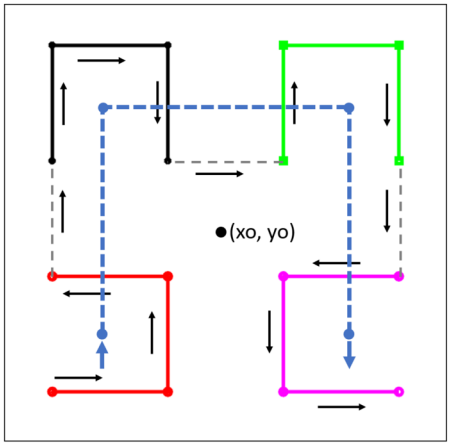

Figure 3 Instance of `generatemotiv()` function appearing in Algorithm 1 in the simplified 2D case. The original leit–motiv (dashed blue line), centered around its pivotal point `(xo,yo)` generates at the successive iteration four leit-motivs in the respective quadrants. For ease of presentation the transformation is depicted in the 2D case, embedded in a square (thin black line). The 3D case is a straightforward extension of this concept

2.1.1 Skeleton metrics

The definition of the backbone picking one of the curves in Γ makes immediate to obtain closed–form skeleton metrics of the vessel ensemble that are relevant for its characterization. Namely, the backbone Γ_n curve is characterized by:

- *length density per unit volume*: since the total length $L(\Gamma_n)$ of the curve is given by

$$L(\Gamma_n) = \frac{(8^n - 1)l}{2^n} \simeq 4^n l, \tag{1}$$

  the *length density per unit volume* is $\simeq 4^n/l^2$
- *extravascular distance*: the points in volume C which realize the maximal distance, say d_n, from the curve are the centers of the leit–motivs. Since these latter have edge $l/2^n$, we have $d_n = \sqrt{3}l/2^{n+1} \simeq l/2^n$
- *curvature and torsion*: curvature and torsion are usually defined and computed for curves of, at least, differentiable of class $\mathcal{C}^1$, *i.e.* that have continuous derivative, which is not the case of the piecewise curves Γ_n. For these curves, the curvature measures the deviation of the curve from a straight line, whilst the torsion measures the deviation of the curve from being plane. The classical generalization of these geometric quantities to polygonal curves refers to closed curves, see *e.g.*, [24]. More recently, a definition has been proposed also in the case of open piecewise linear curves (see [25, 26] and [27]). Here we will follow the notation used in [26, 27]. The *total absolute curvature* (TAC) of a piecewise linear curve of vertices $\{P_i\}$, $i = 0 \dots n$, is the sum of the *turning angles* in each vertex $\{P_i\}$, $i = 1 \dots n-1$, where the turning angle in P_i is the value of the angle $\phi \in [0, \pi]$, between the vectors $\overline{P_{i-1}, P_i}$ and $\overline{P_i, P_{i+1}}$. In the present case, we have
  - $TAC(\Gamma_1(I)) = 6\frac{\pi}{2} = 3\pi$,
  - $TAC(\Gamma_2(I)) = 8TAC(\Gamma_1(I)) + 12\frac{\pi}{2} = 30\pi$, (12 being the number of turning angles arising from the connecting arcs)
  - and for a generic n: $TAC(\Gamma_n(I)) = 8TAC(\Gamma_{n-1}(I)) + 6\pi = \frac{\pi}{7}(27 \cdot 8^{n-1} - 6)$.

  Analogously, we introduce the *total absolute torsion* (TAT) of a piecewise linear curve of vertexes $\{P_i\}$, $i = 0, \dots, n$, considering the tangent and binormal unit vectors

$$\underline{t}_i = \frac{\overline{P_{i-1}, P_i}}{\|\overline{P_{i-1}, P_i}\|}, \qquad \underline{b}_i = \frac{\underline{t}_i \wedge \underline{t}_{i+1}}{\|\underline{t}_i \wedge \underline{t}_{i+1}\|},$$

where $\wedge$ denotes the vector product. Then the TAT is the sum of the angles $\psi \in [0, \pi]$, between the vectors $\underline{b}_i$ and $\underline{b}_{i+1}$, $i = 1 \dots n-2$. In our case, we have:

- $TAT(\Gamma_1(I)) = \pi$,
- $TAT(\Gamma_2(I)) = 8TAT(\Gamma_1(I)) + \pi = 9\pi$,
- $TAT(\Gamma_n(I)) = 8TAT(\Gamma_{n-1}(I)) + \pi = \frac{\pi}{7}(8^n - 1)$.

The above metrical properties of the backbone curve shows that n and l are the characteristic parameters to be chosen in the present model so that artificial networks derived from the above construction reproduce physiological skeleton metrics of capillary networks. We observe that the choice of characteristic parameters is also common to other related works, for example the choice of the density of the number of random Voronoi points used to generate networks in models as in [7, 16] (or the separation distance of the vertices in these models). We also observe that metrics display inter-species variability (*e.g.*, in rat, mouse, cat, human) and even intra-species variability in a relevant range. We consider the following *skeleton metrics*:

- length of a capillary segment (SL)
- length density (LD), *i.e.*, the total capillary length per unit volume
- vertex density (VD), *i.e.*, the number of vertices per unit volume
- maximal and mean distance of the capillaries (MEV, MeaEV) from an internal (non-vascular) point

We studied such metrics for $n = 1, 2, 3$ and for $l = 170$, 160, 150, 125 μm, respectively. The results are shown in Table 1 and the values are to be compared with the reference values shown in Table 2. Setting $n = 2$ allows to better fit the quantities SL, LD, VD, irrespective of the characteristic length l. This latter quantity turns instead to be important when looking at the MEV and MeaEV metrics. The mean distance between capillaries obtained in the artificial network of [16] lays in the range 16-46 μm and it is stated that 73% of the tissue elements are no further than 40 μm away from the nearest blood vessel. In the artificial network of [7], the MeaEV is in the order of 18-20 μm, in the order of 24.2-54.2 μm (cat brain cortex) in [28], 26.02 μm (brain, model) in [17]) and 22-40 μm (human brain, laser microscopy) in [3]). Gathering all these observations, in the following we will set $l = 160$ μm. In Fig. 4, we show for $n = 2$ and $l = 160$ μm the extravascular distances computed numerically and mapped on a vertical and horizontal slice, respectively. The maximal distance is attained in the central region of the leit-motivs and in the region separating different leit-motivs.

3 Geometrical construction of artificial capillary networks: the volumetric construction

Once defined the backbone of the network, we construct its tubular neighborhood to obtain a volumetric structure. To do this, several approaches are possible. In a simplest version – which allows us to perform analytical computations – we consider the union of a family of disks, of given radius r, parametrized by the points of the curve $\Gamma_n(I)$, where each disk is centered in the corresponding point Q of $\Gamma_n(I)$ and belongs to a plane through Q orthogonal to $\Gamma_n(I)$ in Q (sweeping procedure). This construction has to be modified around the vertices P_i where the polygonal backbone curve is not smooth. We approximate the curve around these points by the arc corresponding to a quarter of a circle, with radius R_n, and we sweep along this arc the disk to give a quarter of a torus, with radii r_n and ρ_n, with $r_n + \rho_n = R_n$, respectively (see Fig. 5). In order to obtain, at step n, a global tubular

Table 1 Summary of the skeleton metrics obtained according to choices of the characteristic parameters n and l. Abbreviations: SL = segment length; LD = length density; VD = vertex density; MEV = max extravascular distance, MeaEV = mean extravascular distance

l [μm]	n	SL [μm]	LD [1/mm^2]	VD [#/mm^3]	MEV [μm]	MeaEV [μm]
170						
	1	85	121	1630	69.9	34.3
	2	42.5	545	13,020	33.12	16.7
	3	21.25	2200	10,420		
160						
	1	80	137	1953	65.8	32.2
	2	40	615	15,625	31.17	15.2
	3	20	2495	125,000		
150						
	1	75	155	2370	61.7	30.2
	2	37.5	700	32,476	29.22	15.34
	3	18.75	2840	151,704		
125						
	1	62.5	224	4096	51.4	25.2
	2	31.25	1008	32,760	24.35	12.3
	3	15.625	4088	262,144		

neighborhood Λ_n without self-intersections and having as a centerline the curve $\Gamma_n(I)$, the radii ρ_n and r_n and the length $\frac{l}{2^n}$ of the segment $\overline{P_i, P_{i+1}}$, should satisfy the relations:

$$\text{(i)} \quad \frac{l}{2^n} - 2(r_n + \rho_n) \geq 0, \qquad \text{(ii)} \quad \rho_n \leq \sqrt{2} r_n.$$

For the present range of physiological parameters, condition ii) turns out to be the most restrictive.

3.1 Volume metrics

We are now in a position to compute the volume metrics relevant to the tubular neighborhood, namely its volume and surface. To do this, it is useful to introduce a slight modification of the structure represented in Fig. 5(b), by defining at step n (see Fig. 6):

- T_n each of the red cylinders whose height is $h_n = l_n - 2(r_n + \rho_n)$ and whose radius is r_n
- G_n each of the blue quarters of torus,
- F_n each of the two small yellow cylinders whose height is $r_n + \rho_n$ and whose radius is r_n.

We will denote by Λ'_n the tubular neighborhood with the two cylinders F_n removed.

We have for the portion G_n that its volume is $V(G_n) = \frac{\pi^2}{2}(\rho_n + r_n){r_n}^2$ and its lateral surface $A(G_n) = \pi^2(\rho_n + r_n)r_n$. The final formulas for total volume and lateral area derive from the fact that:

- Λ_1 is composed by 7 cylinders T_1, 6 quarters of torus G_1 and two small cylinders F_1
- Λ_2 is obtained by attaching 8 tubular neighborhoods like Λ'_1 (but in $1:2$ scale) with 7 cylinders of radius r_2 and height $\frac{l}{2^2}$ (composed of one blue cylinder and two yellow ones in $1:2$ scale) and two more cylinders of radius r_2 and height $r_2 + \rho_2$.

In Table 3 we report for the cases $n = 1, 2$ the total volume and lateral area of the network. Observe that in the general case, with similar notations, one can obtain Λ_{n+1} by attaching tubular neighborhoods Λ'_n, in the corresponding scale, with 7 cylinders T_{n+1} and 14 quarters of torus G_{n+1} and two more cylinders F_{n+1}.

Table 2 Skeleton and volume metrics of capillary networks (present work, prior works)

	Units	Present model	Reference data
Vertex density	$\#\cdot 10^3/\text{mm}^3$	15.6	8-11 (mice/human brain, cast [7])
Mean capillary diameter	μm	6	5.9 (human brain, laser microscopy [3]) 4-9 (brain, model [17]) 3.5 ± 0.2 (mouse brain cortex, microscopy, [29])
Total length per unit volume	mm^{-2}	615	370-1090 (cat brain cortex, various refs. in [28]) 469.9 (brain, model [17]) 411-533 (human brain, laser microscopy [3]) 600 (human cortex, model, [16])
Vascular surface per unit volume	mm^{-1}	11.15-10.93	6.2-9.7 (cat brain cortex, various refs. in [28]) 15.3 (cat brain cortex, *ex-vivo* [28]) 9.32 (brain, model [17])
Vascular volume fraction	% of total volume	3.45-3.93	1.4-2.9 (cat brain cortex, various refs. in [28]) 1.54 (brain, model [17]) 2.43-2.45 (human brain, laser microscopy [3]) 0.8-1.5 (mouse brain cortex, microscopy, [29]) 2.49 (human cortex, model, [16])

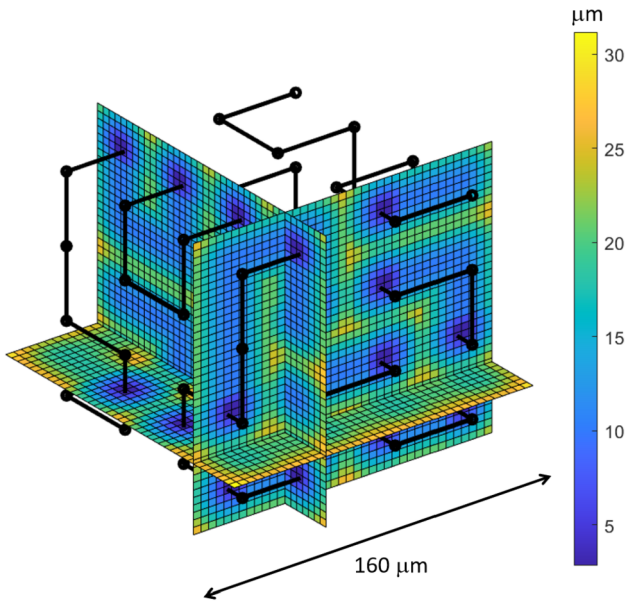

Figure 4 Numerically computed MEV for the backbone generated with $n = 2$ and $l = 160$ μm. Lighter areas represent internal regions with maximal distance from the network

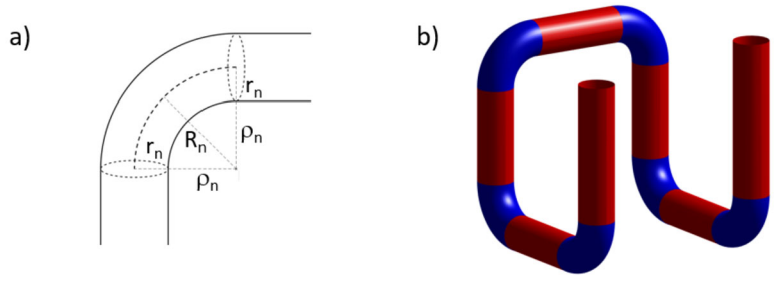

Figure 5 Construction of the tubular neighborhood of the leit-motiv (Γ_1), approximating of the Hilbert curve. (**a**): detail of the procedure near the vertices points of the curve; (**b**) final result, red portions derive from the original leit-motiv, blue portions derive from the toroidal connections

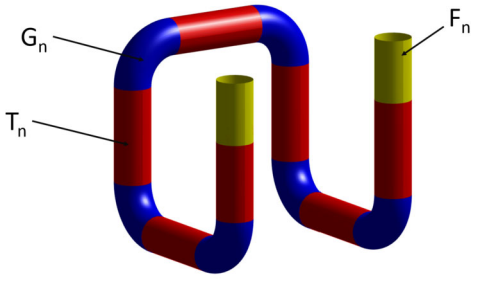

Figure 6 Nomenclature of the portions of the tubular neighborhood of the leit–motiv (used in the nth iteration) useful to compute the volume metrics

We are now in a position to compute the vascular volume fraction and the vascular surface per volume fraction. To do this, we assume a constant tubular radius $r = 3$ μm. In

Table 3 Formulas for the total volume and lateral area of the tubular neighborhood

Iteration #	Volume
1	$\pi r_1^2(18\pi r_1 - 12r_1 + 18\pi\rho_1 + 7\frac{l}{2} - 12\rho_1)$
2	$\pi r_2^2(186\pi r_2 - 124r_2 + 186\pi\rho_2 + 63\frac{l}{4} - 124\rho_2)$
Iteration #	Lateral area
1	$2\pi r_1(3\pi r_1 - 12r_1 + 3\pi\rho_1 + 7\frac{l}{2} - 12\rho_1)$
2	$2\pi r_2(31\pi r_2 - 130r_2 + 31\pi\rho_2 + 65\frac{l}{4} - 130\rho_2)$

Table 2, we summarize all the metric parameters obtained with the present model along with the representative metric parameters from literature (column Reference data). We observe that the curves that we construct in the following sections to obtain more realistic networks, based on the above construction, do not significantly alter these parameters.

4 Realistic capillary networks

In the following, based upon the above construction, we propose a more realistically adherent model of artificial capillary plexum obtained for $n = 2$, $l = 160\ \mu$. To do this first we smooth the backbone via tension spline/Bézier curves of which we can control a tension parameter and then we add segments to include the characteristic presence of loops in capillary plexi.

4.1 Smoothed representation of the backbone

We fit the points generated from points of the generating sequence of the Hilbert curve with a tension spline, and the tension spline is divided by characteristic points, which are then fitted by cubic Bézier curve piece by piece. The tension parameter is a scaling factor such that, the tenser the curve, the more it tends towards straight lines from one point to the next. Several instances of the network are generated by this procedure. The tension is chosen so that the total length – when compared with the total length obtained from Eq. (1) for $n = 2$, given by $\simeq 8^2/2^2 = 15.75$ – displays an increase of about 10-15%.

4.2 Closed loops

The Hilbert curve is a single curve and does not have any branching structure. There are sophisticated manners to represent the branching patterns, for example by reproducing sprouting angiogenesis [13]. In this work, we introduce a more mechanistic approach by making cross-connections between neighboring nodes. To do this, we create the direct graph of the vertices of the backbone curve, then we choose a random set of vertices and for each of them we find the k nearest neighbors via a clustering algorithm. Eventually, we add loops between the vertices of the first set and a subset of the second. Figure 7(a) shows a realization of the network obtained picking 19 (out of 64) vertices and connecting each of them to one of its 4 nearest neighbors. Figure 7(b) shows the graph of the resulting network with the loops. Using the graph of the network, we can count via a numerical procedure the total number of closed loops which are enclosed in the network. For the network represented in Fig. 7 there are 16,514 possible loops. Similar results are obtained with other realizations obtained from curve Γ_2.

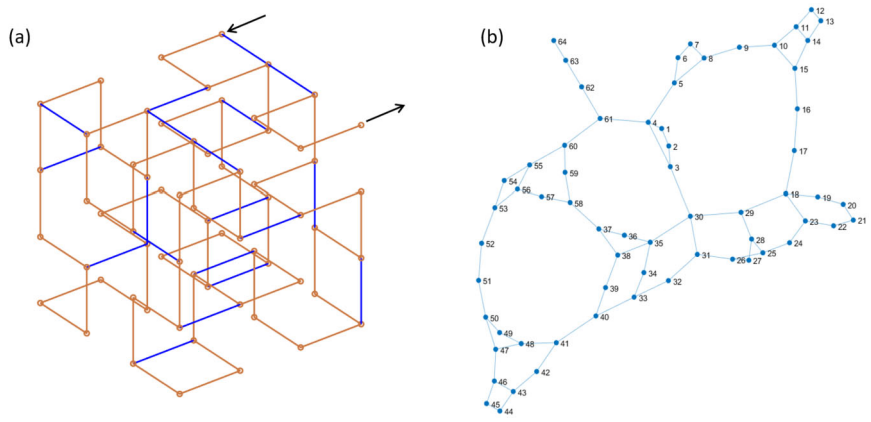

Figure 7 (**a**): realization of a network obtained from the curve Γ_2 upon adding connections (blue segments) to form closed loops. The arrows indicate the original traversal order of the leit-motiv, which is now possibly altered by the presence of loops; (**b**) corresponding graph (numbers indicate the name of the node)

5 Numerical simulations

We consider different instances of the realistic geometry presented in Sect. 4, in turn built upon the backbone of Sect. 2. The cube of length $l = 160\ \mu$m in which the network is embedded conceptually represents a physiological unit of capillary circulation network (the so-called REV). Notice that a similar concept was already used as well in [17] with similar geometric proportions and most recently in [7], in [30] (with a larger dimension) and [31] (with a smaller dimension, and named "3D brain unit"). We perform in this complex domain a 3D numerical simulation of the blood flow, considering the steady incompressible Stokes equations

$$\begin{cases} \nabla \cdot u = 0, \\ \nabla p - \mu \triangle u = 0, \end{cases} \tag{2}$$

where u is the velocity field, p the pressure field, ρ is the blood density and where the blood kinematic viscosity μ is described by a simplified mathematical expression as a function of the vessel radius given by [8]

$$\mu(r) = \frac{\mu_\infty}{(1 + \delta/r)^2},$$

where μ_∞ is the asymptotic viscosity of blood flowing in large tubes and the constant δ is set to 4.29 (r being expressed here in microns). We set $\mu_\infty = 1.09 \cdot \exp(0.024 \cdot \mathrm{Hct})$ where the hematocrit Hct is chosen to be the constant value 0.35 [29]. The problem is numerically solved in COMSOL Multiphysics 5.1 using the built–in $\mathbb{P}_2/\mathbb{P}_1$ finite elements. Boundary conditions are specified in each of the specific test cases.

Test 1 We consider the geometry shown in Fig. 8. At the Inlet 1 (arteriolar input) of the network we set a pressure of 30 mmHg while at the Outlet 1 (venular output) we set a pressure of 15 mmHg. The corresponding pressure drop drives the flow along the network. Figure 8 shows slices of the velocity field magnitude (expressed in m/s) along with the vector field of the blood flow, indicated by the red arrows.

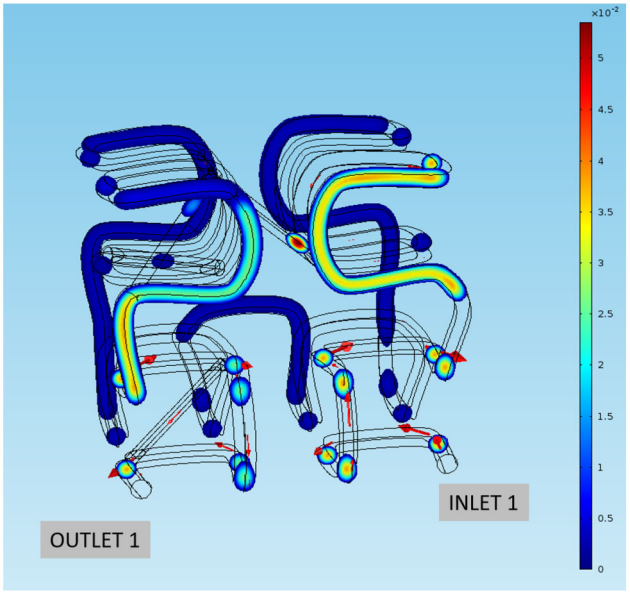

Figure 8 Test 1. Slices of the velocity field magnitude (expressed in m/s) and vector field of the blood flow, indicated by the red arrows

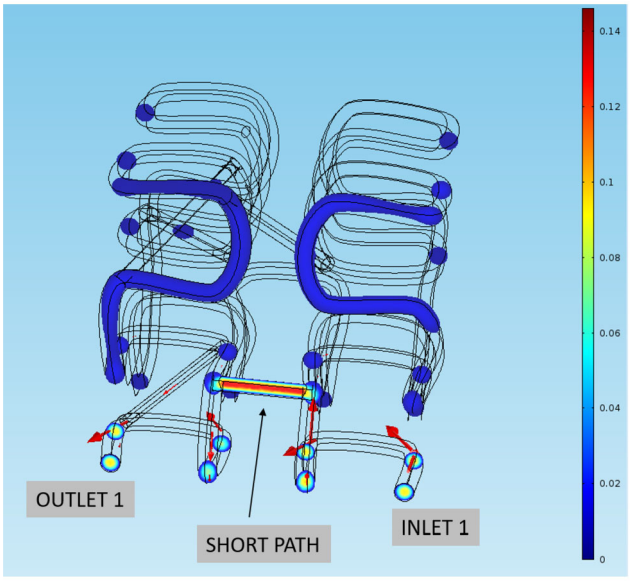

Figure 9 Test 2. Slices of the velocity field magnitude (expressed in m/s) and vector field of the blood flow, indicated by the red arrows. The presence of the shortpath causes the rest of the network to be practically shut off

Test 2 We consider again the geometry shown of Test 1 with the same boundary conditions, and we add a shortpath in the network as indicated in Fig. 9. Observe how in this setting the presence of a short path causes the rest of the network to be practically shut off. Figure 9 shows slices of the velocity field magnitude (expressed in m/s) along with the

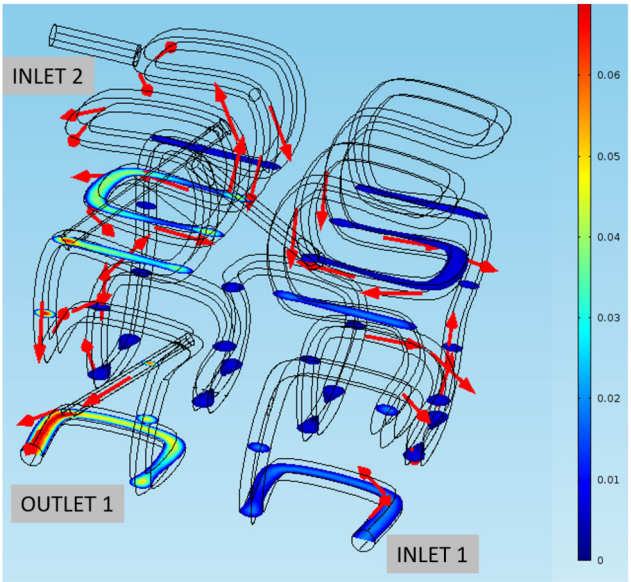

Figure 10 Test 3. Slices of the velocity field magnitude (expressed in m/s) and vector field of the blood flow, indicated by the red arrows. The presence of two inlets causes the merge of two main blood flows which join to reach the outlet with lower pressure

vector field of the blood flow, indicated by the red arrows. Observe how in this setting the presence of the shortpath causes the rest of the network to be practically shut off.

Test 3 Again we consider the same geometry of Test 1 and the same boundary conditions for Inlet 1 and Outlet 1. We add a second arteriolar inlet (Inlet 2), at which we set a blood pressure of 20 mmHg. Figure 10 shows slices of the velocity field magnitude (expressed in m/s) along with the vector field of the blood flow, indicated by the red arrows. Observe how in this setting a more complex blood flow takes place, especially when the flows from the two inputs merge to reach the outlet with lower pressure.

6 Discussion and conclusions

In 1831, M. Hall stated in his book "A Critical and Experimental Essay on the Circulation of the Blood" [32] that "*the number and distribution of the minute and capillary vessels is accurately proportioned and adapted to the object of the circulation*". Over the following two centuries, the significant role of microvascular metrics and topology as determinants of local blood flow has been further emphasized and recognized as an axiomatic denominator of all microcirculatory systems. Vascular geometry has indeed a major impact in the blood dynamics and, in turn, in the origin and development of vascular diseases, through the action of forces exerted by flowing blood on the vascular wall.

Modern medical imaging (CT scan, magnetic resonance, angiography, ...) has made available a good amount of data on the 3D morphology of the *in vivo* microvasculature. Still, real anatomies present very large variability and there is an objective difficulty in retrieving quantitative data from images of microvessels – especially capillary networks – in a robust, operator-independent way. Many post-processing steps (including image segmentation, computation of the centerlines, resolution of branching points) must also

be performed on the raw imaging data with dedicated software in order to obtain tractable geometries. For these reasons, artificial networks with controllable geometric properties and metrics represent appealing tools. A few examples of such constructions have been proposed in literature, mainly based on arrays of parallel/concentric cylinders or Voronoi tessellations, which aim at reproducing – at different degrees of fidelity – a general model of capillary network. In the present work we have introduced a novel approach able to cheaply generate proxy geometries of capillary networks with properties controlled by mathematical parameters. The network backbone was based on approximations of the Hilbert curve, known for its space filling property and skeleton metrics coherent with realistic vascular networks were obtained by tuning the characteristic parameters of the iterative construction n (number of iteration) and l (side of the cell). This construction has naturally embedded the possibility to produce local areas with a higher density of vessels by considering in a target portion successive iterations of the Hilbert curve generation sequence.

The generated coherent geometries have multifold uses. They can serve in numerical simulations as cheap tools to: i) build geometries of representative cells in homogenization procedures. Indeed, when it comes to deal with simulations at the tissue/organ scale, one should resort to reduction techniques in order to obtain a tractable problem [33–35]. In these approaches a detailed microvascular geometry is needed to carry out computations at the single cell level (REV) for further upscaling; ii) generate geometries to be used as training samples in machine learning-based simulations. It is well known indeed the difficulty in the medical field to obtain the large amounts of data required to train neural networks. In this respect, pre-training with artificially generated data, followed by refinement training on a limited number of realistic data, has been shown to be an effective strategy. Having at disposal a mathematical way to generate (and possibly also distort) geometrical configurations at a low cost can play a pivotal role in this kind of approaches. The study of vascular geometry and metrics of microvessel networks can provide by itself indices of specific conditions, or indicate the progression of certain pathologies, as for example in diabetes [36]. This is yet another application where artificially–generated data can be used to pre-train neural networks as surrogates of realistic data to obtain directly usable clinical criteria.

Acknowledgements
Author PC acknowledges the support of the Italian National project MIUR PRIN 2017, Numerical Analysis for Full and Reduced Order Methods for the efficient and accurate solution of complex systems governed by Partial Differential Equations (NA-FROM-PDEs).

Funding
Not applicable.

Abbreviations
REV, Representative Elementary Volume; TAC, total absolute curvature; TAT, total absolute torsion; SL, length of capillary segment; LD, length density; VD, vertex density; MEV, maximal distance of the capillaries (max extravascular distance); MeaV, mean distance of the capillaries (mean extravascular distance).

Availability of data and materials
Not applicable.

Declarations

Ethics approval and consent to participate
Not applicable.

Consent for publication
Not applicable.

Competing interests
The authors declare that they have no competing interests.

Author contributions
All authors conceptualized the work and selected the methodology. MB and CT performed the theoretical construction. PC devised and performed the numerical simulations. All authors carried out the analysis and validation of results. All authors contributed to wrote the paper and approved the final manuscript.

Authors' information
Not applicable.

Publisher's Note

Received: 2 February 2022 Accepted: 20 December 2022 Published online: 02 March 2023

References

1. Tuma RF, Durán WN, Ley K. Microcirculation. San Diego: Academic Press; 2011.
2. Secomb TW. Blood flow in the microcirculation. Annu Rev Fluid Mech. 2017;49(1):443–61. https://doi.org/10.1146/annurev-fluid-010816-060302.
3. Cassot F, Lauwers F, Fouard C, Prohaska S, Lauwers-Cances V. A novel three-dimensional computer-assisted method for a quantitative study of microvascular networks of the human cerebral cortex. Microcirculation. 2006;13(1):1–18.
4. Arciero JC, Causin P, Malgaroli F. Mathematical methods for modeling the microcirculation. Biophysics. 2017;4:362–99.
5. Pan Q, Wang R, Reglin B, Cai G, Yan J, Pries AR, Ning G. A one-dimensional mathematical model for studying the pulsatile flow in microvascular networks. J Biomech Eng. 2014;136(1):011009.
6. Fry BC, Roy TK, Secomb TW. Capillary recruitment in a theoretical model for blood flow regulation in heterogeneous microvessel networks. Physiol Rep. 2013;1(3):e00050.
7. Smith AF, Doyeux V, Berg M, Peyrounette M, Haft-Javaherian M, Larue A-E, Slater JH, Lauwers F, Blinder P, Tsai P et al. Brain capillary networks across species: a few simple organizational requirements are sufficient to reproduce both structure and function. Front Physiol. 2019;10:233.
8. Takahashi T, Nagaoka T, Yanagida H, Saitoh T, Kamiya A, Hein T, Kuo L, Yoshida A. A mathematical model for the distribution of hemodynamic parameters in the human retinal microvascular network. J Biorheology. 2009;23(2):77–86.
9. Ganesan P, He S, Xu H. Development of an image-based network model of retinal vasculature. Ann Biomed Eng. 2010;38(4):1566–85.
10. Su S-W, Catherall M, Payne S. The influence of network structure on the transport of blood in the human cerebral microvasculature. Microcirculation. 2012;19(2):175–87.
11. Levine HA, Pamuk S, Sleeman BD, Nilsen-Hamilton M. Mathematical modeling of capillary formation and development in tumor angiogenesis: penetration into the stroma. Bull Math Biol. 2001;63(5):801–63.
12. Sefidgar M, Soltani M, Raahemifar K, Sadeghi M, Bazmara H, Bazargan M, Naeenian MM. Numerical modeling of drug delivery in a dynamic solid tumor microvasculature. Microvasc Res. 2015;99:43–56.
13. Alberding JP, Secomb TW. Simulation of angiogenesis in three dimensions: application to cerebral cortex. PLoS Comput Biol. 2021;17(6):1009164.
14. Reichold J, Stampanoni M, Keller AL, Buck A, Jenny P, Weber B. Vascular graph model to simulate the cerebral blood flow in realistic vascular networks. J Cereb Blood Flow Metab. 2009;29(8):1429–43.
15. El-Bouri WK, Payne SJ. Multi-scale homogenization of blood flow in 3-dimensional human cerebral microvascular networks. J Theor Biol. 2015;380:40–7.
16. Linninger A, Gould I, Marinnan T, Hsu C-Y, Chojecki M, Alaraj A. Cerebral microcirculation and oxygen tension in the human secondary cortex. Ann Biomed Eng. 2013;41(11):2264–84.
17. Safaeian N, David T. A computational model of oxygen transport in the cerebrocapillary levels for normal and pathologic brain function. J Cereb Blood Flow Metab. 2013;33(10):1633–41.
18. Gould IG, Linninger AA. Hematocrit distribution and tissue oxygenation in large microcirculatory networks. Microcirculation. 2015;22(1):1–18.
19. Lorthois S, Cassot F, Lauwers F. Simulation study of brain blood flow regulation by intra-cortical arterioles in an anatomically accurate large human vascular network. Part ii: flow variations induced by global or localized modifications of arteriolar diameters. NeuroImage. 2011;54(4):2840–53.
20. Sagan H. Space-filling curves. Berlin: Springer; 2012.
21. Haverkort H. How many three-dimensional Hilbert curves are there? 2016. arXiv preprint arXiv:1610.00155.
22. Forte F. Hilbert curve. 2020. https://www.mathworks.com/matlabcentral/fileexchange/4646-hilbert-curve.
23. Martynov I. Hilbert3(n). (2020). https://www.mathworks.com/matlabcentral/fileexchange/25348-hilbert3-n.
24. Milnor JW. On the total curvature of knots. Ann Math. 1950;52(2):248–57.
25. Enomoto K, Itoh J-i. The total absolute curvature and the total absolute torsion of open curves in the Euclidean spaces. In: Recent advances in the geometry of submanifolds: dedicated to the memory of Franki Dillen (1963–2013). Contemp. Math. vol. 674. Providence: Am. Math. Soc.; 2016. p. 41–8.
26. Mucci D, Saracco A. The weak Frénet frame of non-smooth curves with finite total curvature and absolute torsion. Ann Mat Pura Appl. 2020;199:2459–88.
27. Sullivan JM. Curves of finite total curvature. In: Discrete differential geometry. Berlin: Springer; 2008. p. 137–61.

28. Pawlik G, Rackl A, Bing RJ. Quantitative capillary topography and blood flow in the cerebral cortex of cats: an in vivo microscopic study. Brain Res. 1981;208(1):35–58.
29. Gould IG, Tsai P, Kleinfeld D, Linninger A. The capillary bed offers the largest hemodynamic resistance to the cortical blood supply. J Cereb Blood Flow Metab. 2017;37(1):52–68.
30. Possenti L, di Gregorio S, Gerosa FM, Raimondi G, Casagrande G, Costantino ML, Zunino P. A computational model for microcirculation including Fahraeus-Lindqvist effect, plasma skimming and fluid exchange with the tissue interstitium. Int J Numer Methods Biomed Eng. 2019;35(3):3165.
31. Vendel E, Rottschäfer V, De Lange EC. A 3D brain unit model to further improve prediction of local drug distribution within the brain. PLoS ONE. 2020;15(9):0238397.
32. Hall MEA. A critical and experimental essay on the circulation of the blood; especially as observed in the minute aud capillary vessels of the Batrachia and of fishes. London: Seeley & Burnside; 1832.
33. Penta R, Ambrosi D. The role of the microvascular tortuosity in tumor transport phenomena. J Theor Biol. 2015;364:80–97.
34. Shipley RJ, Sweeney PW, Chapman SJ, Roose T. A four-compartment multiscale model of fluid and drug distribution in vascular tumours. Int J Numer Methods Biomed Eng. 2020;36(3):3315.
35. Cattaneo L, Zunino P. A computational model of drug delivery through microcirculation to compare different tumor treatments. Int J Numer Methods Biomed Eng. 2014;30(11):1347–71.
36. Piccinelli M, Veneziani A, Steinman DA, Remuzzi A, Antiga L. A framework for geometric analysis of vascular structures: application to cerebral aneurysms. IEEE Trans Med Imaging. 2009;28(8):1141–55.